

# Exclusion of the Cosmological Triangle in Reactor-Based Search for Axion-Like Particles

Byung Ju Park,<sup>1,2</sup> Jae Jin Choi,<sup>3,2</sup> Eunju Jeon,<sup>2,1</sup> Jinyu Kim,<sup>4</sup> Kyungwon Kim,<sup>2</sup> Sung Hyun Kim,<sup>2</sup>  
Sun Kee Kim,<sup>3</sup> Yeongduk Kim,<sup>2,1</sup> Young Ju Ko,<sup>2</sup> Byoung-Cheol Koh,<sup>5</sup> Chang Hyon Ha,<sup>5</sup> Seo  
Hyun Lee,<sup>1,2</sup> In Soo Lee,<sup>2,\*</sup> Hyunseok Lee,<sup>1,2</sup> Hyun Su Lee,<sup>2,1,†</sup> Jaison Lee,<sup>2</sup> and Yomin Oh<sup>2</sup>  
(NEON Collaboration)

Doojin Kim<sup>6</sup>

<sup>1</sup>*IBS School, University of Science and Technology (UST), Daejeon 34113, Republic of Korea*

<sup>2</sup>*Center for Underground Physics, Institute for Basic Science (IBS), Daejeon 34126, Republic of Korea*

<sup>3</sup>*Department of Physics and Astronomy, Seoul National University, Seoul 08826, Republic of Korea*

<sup>4</sup>*HANARO Utilization Division, Korea Atomic Energy Research Institute (KAERI), Daejeon 34057, Republic of Korea*

<sup>5</sup>*Department of Physics, Chung-Ang University, Seoul 06973, Republic of Korea*

<sup>6</sup>*Mitchell Institute for Fundamental Physics and Astronomy,*

*Department of Physics and Astronomy, Texas A&M University, College Station, TX 77845, USA*

(Dated: June 13, 2024)

We report new constraints on axion-like particle (ALP) using data corresponding to a sodium iodine target exposure of 3063 kg-days from the neutrino elastic scattering observation with NaI (NEON) experiment. A 16.7 kg of thallium-doped sodium iodide target was located 23.7 meters from a 2.8 GW thermal power nuclear reactor. We searched for ALPs produced by high-flux photons by comparing the energy spectra of data collected during reactor-on (1596 kg-days exposure) and reactor-off (1467 kg-days exposure) periods. No signal consistent with ALP interaction was identified, allowing us to set exclusion limits at the 95% confidence level. Our limits cover previously unexplored regions for both photon couplings ( $g_{a\gamma}$ ) and electron couplings ( $g_{ae}$ ) for axion masses around 1 MeV/c<sup>2</sup>. Notably, the NEON data excludes the unconstrained region identified by laboratory-based searches for photon couplings within the “cosmological triangle” for the first time. The observed 95% confidence level limits reach as low as  $g_{a\gamma}$  of  $4.33 \times 10^{-8} \text{ GeV}^{-1}$  and  $g_{ae}$  of  $1.10 \times 10^{-9}$  for axion masses of 1.7 MeV/c<sup>2</sup> and 1.0 MeV/c<sup>2</sup>, respectively.

## INTRODUCTION

Axions are hypothetical particles first proposed in 1977 by Peccei and Quinn [1] to address the strong  $CP$  problem in quantum chromodynamics (QCD) [2, 3]. Due to their extremely light mass and weak interaction with ordinary matter, axions are considered excellent candidates for dark matter [4–6]. Despite numerous experimental searches, axions have not been detected so far [7–10]. The concept has been extended to include axion-like particles (ALPs) in various models [11, 12]. While ALPs share many properties with axions, making them viable dark matter candidates, they are not specifically tied to solving the strong  $CP$  problem. These particles can have a wide range of masses and coupling constants, leading to diverse phenomenological implications in both astrophysical and laboratory contexts [12].

ALPs can interact with Standard Model leptons and the electromagnetic field, prompting extensive experimental searches [10]. Light ALPs (mass below 100 keV/c<sup>2</sup>) are typically probed by solar helioscope, haloscope, or photon regeneration experiments [13]. In contrast, heavy ALPs (mass above 100 keV/c<sup>2</sup>) are investigated using colliders or beam-dump experiments [14]. Astrophysical observations provide complementary constraints on the ALP parameter space [15]. Notably, a region with ALP mass ( $m_a$ ) around 0.5–5 MeV/c<sup>2</sup>

and axion-photon coupling constant ( $g_{a\gamma}$ ) around  $2 \times 10^{-6} - 3 \times 10^{-5} \text{ GeV}^{-1}$  remains unexplored by direct searches and the astrophysical bounds. This region, known as the “cosmological triangle” [16, 17], was previously accessible only through model-dependent cosmological arguments [18, 19]. Increasing interest in exploring this region [17] has led to studies suggesting the potential for ALP searches using short-baseline reactor experiments [20, 21], the accelerator-based CCM experiment with a 10-ton liquid argon target [22], DUNE-like future neutrino experiment with a 50-ton liquid argon or gases argon [16], and a 2-kton liquid scintillator with an intense proton beam underground [23].

Nuclear reactors are the most intense sources of photons with energies up to a few MeV. Since ALPs can be produced via photon-induced scattering [12], reactors offer a promising avenue for searching for ALPs in the MeV/c<sup>2</sup> mass range. Here, we present the first direct search for ALPs using the NEON experiment. By leveraging the intense MeV/c<sup>2</sup> mass ALP productions from the reactor core, the NEON experiment, with a target mass of only 16.7 kg of thallium doped sodium iodine (NaI(Tl)) crystals, covers the “cosmological triangle” for the first time through laboratory-based searches.

## NEON EXPERIMENT

The NEON experiment is designed to detect neutrino-nucleus coherent scattering (CE $\nu$ NS) using reactor electron antineutrinos [24]. The detector is located in the tendon gallery of the 2.8 GW Hanbit nuclear power reactor,  $23.7 \pm 0.3 \text{ m}$

\* islee@ibs.re.kr

† hyunsulee@ibs.re.kr

away from the center of the reactor core. After an engineering run in 2021, the detector encapsulation was upgraded to improve long-term operational stability [25]. Additionally, two small-size detector modules were replaced with large-size ones, resulting in a total crystal mass of 16.7 kg.

The six NaI(Tl) modules are submerged in 800 liters of liquid scintillator. This liquid scintillator helps identify and reduce radioactive backgrounds affecting the NaI(Tl) crystals [26]. To further reduce external radiation background, the liquid scintillator is surrounded by shielding made of lead, borated polyethylene, and high-density polyethylene [24] (see also Fig. A1).

Each NaI(Tl) crystal is directly coupled to two photomultiplier tubes (PMTs) without quartz window for enhanced light collection efficiency [27]. The crystal and PMTs assembly is encapsulated with a copper casing [25]. A trigger is generated when a signal corresponding to one or more photoelectrons occurs in each PMT within a 200 ns time window. Two readouts of a high-gain signal from the anode for 0–60 keV energy range and a low-gain signal from the 5<sup>th</sup>-stage dynode for 60–3000 keV range are independently recorded as 8  $\mu$ s waveforms, a similar system to that used by the COSINE-100 experiment [28]. To reject unwanted phosphorescence events from direct muon hit events, a 300 ms dead time for high energy events with approximately 3 MeV threshold is applied.

The data used in this analysis were acquired between April 11, 2022 and June 22, 2023, for a total live time exposure of 5702 kg-days. Between September 26, 2022 and February 22, 2023, the reactor was inactive for regular maintenance and fuel replacement. The reactor operated at full power for the remaining period. A few data acquisition (DAQ) downtimes occurred due to unexpected power outages, resulting in a DAQ efficiency of approximately 70% during whole period.

Although this analysis focused on 3–3000 keV energy events, we used the same good-quality data for the low-energy CE $\nu$ NS search analysis, as the low-energy (<3 keV) background could be more precisely understood through high-energy backgrounds [29]. We employed a boosted decision tree (BDT)-based multi-variable machine learning technique [30] to reject PMT-induced noise contamination. We have monitored the event rate with BDT-based selection criteria in the 1–3 keV energy region to determine a data quality of each one hour dataset for each detector. Depending on the crystal, approximately 35% of the data was excluded due to persistent high PMT-induced noise rates. Notably, the entire dataset from detector-3 was excluded. This resulted in effective exposure times of 1596 kg-days and 1467 kg-days for the reactor-on and reactor-off periods, respectively (see also Table A1 and Fig. A2).

ALP search candidate events were selected based on the following criteria. Energy above 3 keV (avoid PMT-induced noise events) and below 3 MeV (considering the DAQ system’s dynamic range limit) was required. Rejection of  $\alpha$  events in the crystals using pulse shape discrimination [24] was applied. Events coincident with the liquid scintillator deposited energies above 5 MeV were rejected as muon candidate events. Selected events were further categorized as single-hit or multiple-hit events. A multiple-hit event has ac-

companying crystal signals with more than four photoelectrons or a liquid scintillator signal above 80 keV within 150 ns time coincidence window. All other events were classified as a single-hit sample.

Most background contributions in the NaI(Tl) detectors remain stable over a two-year data acquisition period [29]. Although the dominant  $^{210}\text{Pb}$  contamination has a half-life of 22.3 years, its variation during the two-year data period is negligible. We thus define the effectively time-independent background components as the “Continuum background”, which includes internal contaminants, surface contamination, and external radiation, with a half-life equal to or greater than that of  $^{210}\text{Pb}$ . In addition to the continuum background, we identified a few time-dependent backgrounds. Short-lived cosmogenic contaminants in the NaI(Tl) crystals due to cosmic ray exposure prior to the detector installation are understood by dedicated analysis [31]. Seasonal variations in  $^{222}\text{Rn}$  levels, with higher levels observed in summer due to temperature changes [32], can affect the time-dependent background. Dust contamination introduced during detector upgrades, containing long-lived isotopes, which settled to the bottom of the liquid scintillator over time, produced a decreased rate over time. Figure 1 (A) and (B) show example data for single-hit events in detector-6 compared to the expected backgrounds (see also Fig. A3 for the multiple-hit events).

We modeled time-dependent background contributions by dividing the data into seven different time periods, each two months long (see Fig. A4), and extracted the  $^{222}\text{Rn}$  and dust contributions (see Fig. A5). This model enable us to understand the remaining background in the reactor-on-minus-off dataset, as shown in Fig. 1 (C) (see also Fig. A3 (C)). The measured data are well described by the expected backgrounds. The ALP signal would only be produced during reactor operation indicated by red lines in Fig. 1.

With a proper model of the expected background and the reactor-on-minus-off spectra as seen in Fig. 1, data spectra for ALP searches can be prepared. Considering the varying event rates across different energy ranges, we employed dynamic energy bins ranging from 57 keV (3–60 keV) to 600 keV (2400 keV–3000 keV). Figure 2 presents the ALP search data from detector-6, based on the reactor-on-minus-off spectra, where both single-hit and multiple-hit channels are used simultaneously.

Several sources of systematic uncertainty are included in our modeling of the reactor-on-minus-off spectra. These include potential variations in detector responses between the reactor-on period and the reactor-off periods. The largest systematic uncertainties are associated with the time-dependent background modeling of  $^{222}\text{Rn}$  variation, U and Th amounts in the dust. Additionally, a possible contamination of  $^{222}\text{Rn}$  into the liquid scintillator and different location of the dust also contributes to systematic uncertainties. Figure 2 indicates systematic uncertainty bands for the expected background.

## ALP SEARCHES

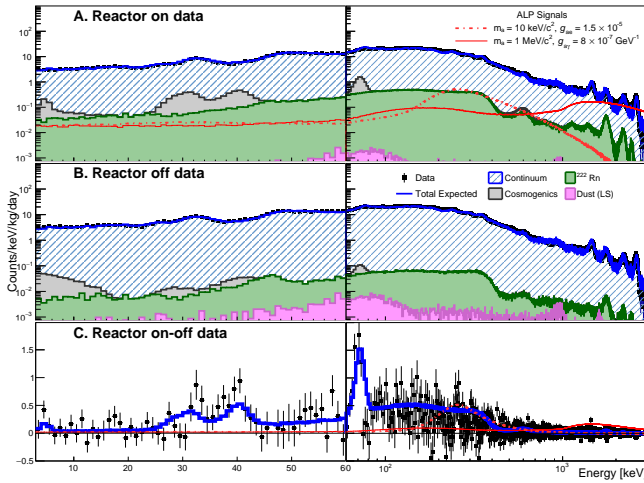


Fig. 1. **Single-hit energy spectra of detector-6 module.** This figure shows the normalized energy spectra of the single-hit events (black points) in the detector-6 module. The spectra are compared with the expected background contributions (blue solid lines) for both the reactor-on state (A) and the reactor-off state (B). The expected background includes contributions from time-independent continuum components and time-dependent components of cosmogenic activation,  $^{222}\text{Rn}$  in the calibration holes, and  $^{238}\text{U}$   $^{232}\text{Th}$  from the dust contamination in the liquid scintillator. For the reactor-on data (A), two benchmark ALP signals of  $m_a = 10 \text{ keV}/c^2$ ,  $g_{ae} = 1.5 \times 10^{-5}$  (red dashed line) and  $m_a = 1 \text{ MeV}/c^2$ ,  $g_{a\gamma} = 8 \times 10^{-7} \text{ GeV}^{-1}$  (red solid line) are included. (C) shows the reactor-on-minus-off data spectrum with the expected background (blue solid line) and the same two benchmark ALP signals.

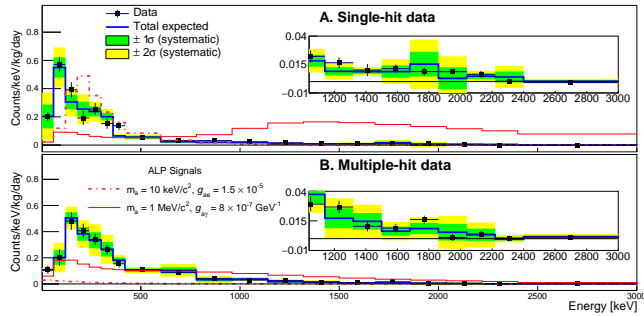


Fig. 2. **ALP search data from detector-6 module.** This figure present the reactor-on-minus-off data spectra used for ALP signal searches in detector-6 module. The data is shown for both single-hit (A) and multiple-hit (B). The data points (black circles) and the expected background spectra (blue solid lines) are derived from the models presented in Fig. 1 (single-hit) and Fig. A3 (multiple-hit), but with different bin sizes used for this analysis. The green and yellow bands indicate 68% and 95% confidence level intervals for the background model, respectively. The inset zooms in on the high-energy region for better visibility. Two benchmark ALP signals are overlaid for comparison:  $m_a = 10 \text{ keV}/c^2$ ,  $g_{ae} = 1.5 \times 10^{-5}$  (red dashed line) and  $m_a = 1 \text{ MeV}/c^2$ ,  $g_{a\gamma} = 8 \times 10^{-7} \text{ GeV}^{-1}$  (red solid line).

Intense photons are generated in the nuclear reactor through nuclear fission, the decay of fission products, capture processes, decay of capture products, and scattering [33], with the photon flux approximated from the FRJ-1 research reactor [34]. We focus on a generic model of an ALP coupled to either a photon or electron. For photon coupling, ALPs can be produced through the Primakoff process ( $\gamma + N \rightarrow a + N$ ), where a photon ( $\gamma$ ) interacts with a nucleus ( $N$ ) to produce an axion ( $a$ ) [35]. Detection occurs through two-photon pair production ( $a \rightarrow \gamma\gamma$ ) or the inverse Primakoff process, with the rate depending on the strength of the axion-photon coupling constant  $g_{a\gamma}$ . For electron coupling, ALPs can occur through the Compton-like process ( $\gamma + e^- \rightarrow a + e^-$ ) and be detected through electron-positron pair production ( $a \rightarrow e^-e^+$ ), axio-electric absorption ( $a + e^- + N \rightarrow e^- + N$ ), or inverse Compton-like process ( $a + e^- \rightarrow \gamma + e^-$ ). The rate of these processes depends on the strength of the axion-electron coupling constant  $g_{ae}$ . Two benchmark signals of the axion-photon coupling ( $m_a = 1 \text{ MeV}/c^2$ ,  $g_{a\gamma} = 8 \times 10^{-7} \text{ GeV}^{-1}$ ) and the axion-electron coupling ( $m_a = 10 \text{ keV}/c^2$ ,  $g_{ae} = 1.5 \times 10^{-5}$ ) are used for comparison with the measured data spectra in Fig. 1 and Fig. 2. We do not consider the ALP production through the nuclear de-excitation, as studied by the TEXONO experiment [36].

The NEON data are fitted for each ALP mass and interaction type. We use various simulated ALP signals to evaluate their potential contributions to the measured energy spectra of the reactor-on-minus-off data (shown in Fig. 2). A  $\chi^2$  fit is applied to the measured spectra (both single-hit and the multiple-hit channels) between 3 and 3,000 keV for each ALP signal and various ALP masses. Each crystal and channel is fitted with a crystal-channel specific background model and a crystal-channel correlated ALP signal. The combined fit is achieved by summing the  $\chi^2$  values from the five crystals and two channels.

An example of a  $\chi^2$  fit for the axion-photon coupling with a  $1 \text{ MeV}/c^2$  ALP mass is presented in Fig. 3 for both single-hit (A) and multiple-hit (B) events. The averaged energy spectra for the five crystals are shown along with the best-fit results. For comparison, the expected signals for a  $g_{a\gamma} = 3.1 \times 10^{-7} \text{ GeV}^{-1}$ , which is 10 times higher signal rates of the 95% confidence level upper limit of a  $g_{a\gamma} = 9.7 \times 10^{-8} \text{ GeV}^{-1}$ , are also included. No statistically significant excess of events is found for any of the considered ALP signals. The posterior probabilities of the signals are consistent with zero in all cases, and 95% confidence level limits are determined.

## RESULTS AND DISCUSSION

Figure 4 shows 95% confidence level exclusion limits derived from NEON data for ALPs coupled solely to photons. These limits are presented in the two dimensional parameter space of ALP mass ( $m_a$ ) and ALP-photon coupling constant ( $g_{a\gamma}$ ). For ALP mass below  $20 \text{ keV}/c^2$ , the dominant

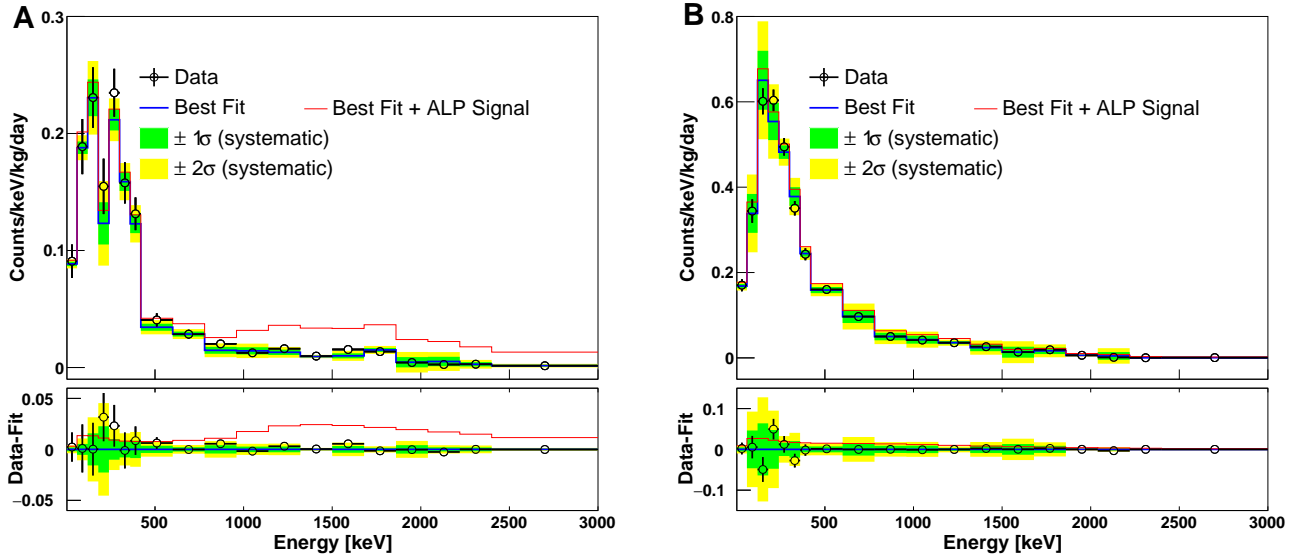


Fig. 3.  $\chi^2$  fit results for axion-photon coupling ( $m_a=1 \text{ MeV}/c^2$ ). The data points (black circles with error bars) represent the summed energy spectra from the five crystals on the normalized reactor-on-minus-off data. The blue solid lines represent the best-fit results for the  $1 \text{ MeV}/c^2$  ALP mass assuming axion-photon coupling. (A) corresponds to single-hit and (B) corresponds to multiple-hit events. The expected signal excess above background for a  $1 \text{ MeV}/c^2$  mass and  $g_{a\gamma} = 3.1 \times 10^{-7} \text{ GeV}^{-1}$ , which is 10 times higher signal rate than the 95% confidence level upper limit of  $g_{a\gamma} = 9.7 \times 10^{-8} \text{ GeV}^{-1}$ , is shown in red solid lines. The green (yellow) bands are the 68% (95%) confidence level intervals for the background model fits. The lower panels show the data minus best-fit residuals.

contribution arises from the scattering process via inverse Primakoff process. At higher ALP masses, the limit is set by the  $a \rightarrow \gamma\gamma$  decay process. Since this decay can happen during the 23.7 meters flight, we consider limits for both lower and higher  $g_{a\gamma}$  values. The sensitivity of the search weakens for ALP masses exceeding approximately  $3 \text{ MeV}/c^2$ . This arises from the limited energy range (up to  $3 \text{ MeV}$ ) of our analysis due to detector saturation for high-energy events and reduced photon flux for higher energy. However, we can still search for higher-mass ALPs by looking for signatures of Compton scattering. In this process, a high-energy photon interacts with the ALP, depositing a lower-energy electron or photon within our detectable range. Future improvements involving the reconstruction of the saturated events, similar to techniques used in the COSINE-100 experiment for boosted dark matter searches [37], could enhance the sensitivity of our ALP search for high masses.

The exclusion limits presented in Fig. 4 extend beyond previously unexplored regions of the ALP parameter space compared to existing constraints from beam dump experiments, astrophysical and cosmological limits adapted from Refs. [38, 39]. Notably, this study excludes the most of “cosmological triangle”, a previously unconstrained region uncovered by beam dump experiment and the astrophysical bounds. Small remained region of KSVZ QCD axion model parameter space [40] in the axion mass about a few  $100 \text{ keV}/c^2$  was fully ruled out.

Figure 5 shows the 95% confidence level exclusion limit from ALPs coupled purely to electrons, again presented in  $m_a$ - $g_{ae}$  parameter space. For the ALP masses below

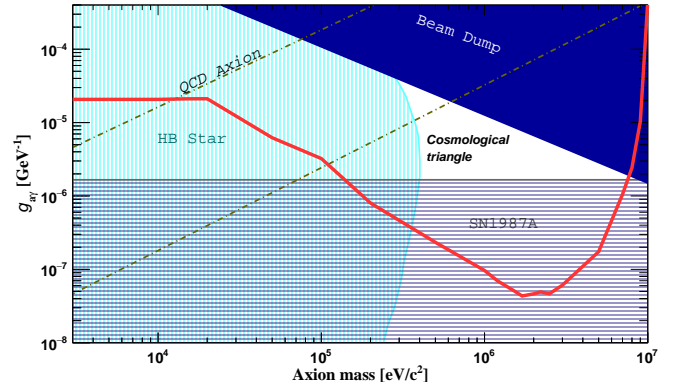


Fig. 4. **Exclusion limit on the axion-photon coupling.** The observed 95% confidence level exclusion limit (red solid line) derived from NEON data for the axion-photon is compared with limits from beam dump experiments [41, 42], SN1987A [43, 44], and HB stars cooling arguments [45]. This limit covers the remained QCD axion parameter space predicted by the KSVZ model [40] for the axion mass around a few  $100 \text{ keV}/c^2$ .

$1.0 \text{ MeV}/c^2$ , the limits are set by scattering processes via inverse Compton-like process and axio-electric absorption. Limit for higher ALP masses ( $m_a > 1.0 \text{ MeV}/c^2$ ) are dominated by  $a \rightarrow e^+e^-$  decay process, which has a kinematic limit of  $m_a > 2m_e = 1.0 \text{ MeV}/c^2$  (where  $m_e$  is the electron mass). Similar to the ALP-photon case, we consider limits for both upper and lower bounds due to the ALP decay during

flight.

The NEON data covers previously explored regions by Stellar cooling arguments [15] for axion mass less than  $300 \text{ keV}/c^2$ , where environmental effects could allow circumventing those limit [21]. In the mass range between  $300 \text{ keV}/c^2$  and  $1.0 \text{ MeV}/c^2$ , the scattering process search probes regions of coupling down to  $g_{ae}$  about  $4 \times 10^{-6}$ , which were previously unexplored by either direct searches or astrophysical and cosmological considerations. This limit reaches into parts of the QCD axion parameter space predicted by the DFSZ-I models [40]. For the ALP masses above the kinematic limit for  $a \rightarrow e^+e^-$  ( $m_a > 1.0 \text{ MeV}/c^2$ ), the NEON data competes with limits from the beam dump experiments [46–48]. However, our limits extend to lower  $g_{ae}$  values (down to  $10^{-9}$ ) in this region, representing the first such constraints from a laboratory experiment. The ALP search for the axion-electron coupling using NEON data is limited for ALP masses below  $1.6 \text{ MeV}/c^2$  due to the  $3 \text{ MeV}$  dynamic range of the detector. Similar to the ALP-photon case, reconstruction of saturated events above  $3 \text{ MeV}$  energies could extend the search to higher ALP masses, as demonstrated in Ref. [21].

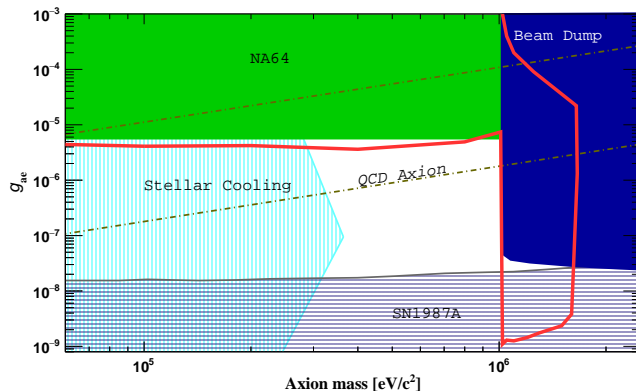


Fig. 5. **Exclusion limit on the axion-electron coupling.** The observed 95% confidence level exclusion limit (red solid line) on the axion-electron coupling derived from the NEON data is compared with limits from beam dump experiments [46–48], SN1987A [49], Stellar cooling [50] and NA64 missing energy search [51]. QCD axion model parameter space for the DFSZ(I) benchmark scenario span the regions indicated by the gray dashed lines [40].

## CONCLUSION

This work presents the first direct search for axion-like particles (ALPs) using the NEON experiment. NEON leverages  $16.7 \text{ kg}$  NaI(Tl) crystal detectors positioned  $23.7 \text{ meters}$  away from a  $2.8 \text{ GW}$  thermal power reactor core. The analysis of NEON data has yielded new exclusion limits for ALPs coupled to both photons and electrons. These limits reveal previously unexplored regions in the ALP mass range around  $1 \text{ MeV}/c^2$  for both coupling scenarios. Significantly, this work is the first laboratory experiment to mostly rule out the “cosmological triangle” of ALP-photon couplings, a previous unconstrained region. The intense photon (or ALP) flux from the reactor, combined with precise background understanding and a low event rate in the signal regions, enabled this significant achievement. Furthermore, ongoing data collection and efforts to lower the energy threshold for  $\text{CE}\nu\text{NS}$  search, as well as to reconstruct events above  $3 \text{ MeV}$ , hold promise for improving future ALP searches. These advancements could provide even more stringent constraints and a deeper understanding of ALP properties.

## ACKNOWLEDGMENTS

We thank the Korea Hydro and Nuclear Power (KHNP) company for the help and support provided by the staff members of the Safety and Engineering Support Team of Hanbit Nuclear Power Plant 3 and the IBS Research Solution Center (RSC) for providing high performance computing resources. This work is supported by the Institute for Basic Science (IBS) under Project Code IBS-R016-A1 and the National Research Foundation (NRF) grant funded by the Korean government (MSIT) (NRF-2021R1A2C1013761 and NRF-2021R1A2C3010989), Republic of Korea.

- 
- [1] R. D. Peccei and H. R. Quinn, CP Conservation in the Presence of Instantons, *Phys. Rev. Lett.* **38**, 1440–1443 (1977).
  - [2] F. Wilczek, Problem of Strong  $P$  and  $T$  Invariance in the Presence of Instantons, *Phys. Rev. Lett.* **40**, 279–282 (1978).
  - [3] S. Weinberg, A New Light Boson?, *Phys. Rev. Lett.* **40**, 223–226 (1978).
  - [4] J. Preskill, M. B. Wise, and F. Wilczek, Cosmology of the Invisible Axion, *Phys. Lett. B* **120**, 127–132 (1983).
  - [5] L. F. Abbott and P. Sikivie, A Cosmological Bound on the Invisible Axion, *Phys. Lett. B* **120**, 133–136 (1983).
  - [6] M. Dine and W. Fischler, The Not So Harmless Axion, *Phys. Lett. B* **120**, 137–141 (1983).
  - [7] C. Bartram et al., (ADMX Collaboration), Search for Invisible Axion Dark Matter in the  $3.3\text{--}4.2 \mu\text{eV}$  Mass Range, *Phys. Rev. Lett.* **127**, 261803 (2021).
  - [8] K. M. Backes et al., (HAYSTAC Collaboration), A quantum-enhanced search for dark matter axions, *Nature* **590**, 238–242 (2021).
  - [9] O. Kwon et al., (CAPP Collaboration), First Results from an Axion Haloscope at CAPP around  $10.7 \mu\text{eV}$ , *Phys. Rev. Lett.* **126**, 191802 (2021).
  - [10] R. L. Workman et al., (Particle Data Group Collaboration), Review of Particle Physics, *PTEP* **2022**, 083C01 (2022).

- [11] E. Witten, Some Properties of O(32) Superstrings, *Phys. Lett. B* **149**, 351–356 (1984).
- [12] K. Choi, S. H. Im, and C. Sub Shin, Recent Progress in the Physics of Axions and Axion-Like Particles, *Ann. Rev. Nucl. Part. Sci.* **71**, 225–252 (2021).
- [13] Y. K. Semertzidis and S. Youn, Axion dark matter: How to see it?, *Sci. Adv.* **8**, abm9928 (2022).
- [14] F. Capozzi, B. Dutta, G. Gung, W. Jang, I. M. Shoemaker, A. Thompson, and J. Yu, New constraints on ALP couplings to electrons and photons from ArgoNeUT and the MiniBooNE beam dump, *Phys. Rev. D* **108**, 075019 (2023).
- [15] G. G. Raffelt, Astrophysical axion bounds, *Lect. Notes Phys.* **741**, 51–71 (2008).
- [16] V. Brdar, B. Dutta, W. Jang, D. Kim, I. M. Shoemaker, Z. Tabrizi, A. Thompson, and J. Yu, Axionlike Particles at Future Neutrino Experiments: Closing the Cosmological Triangle, *Phys. Rev. Lett.* **126**, 201801 (2021).
- [17] G. Lucente, O. Straniero, P. Carezza, M. Giannotti, and A. Mirizzi, Constraining Heavy Axionlike Particles by Energy Deposition in Globular Cluster Stars, *Phys. Rev. Lett.* **129**, 011101 (2022).
- [18] P. F. Depta, M. Hufnagel, and K. Schmidt-Hoberg, Updated BBN constraints on electromagnetic decays of MeV-scale particles, *JCAP* **04**, 011 (2021).
- [19] A. Caputo, G. Raffelt, and E. Vitagliano, Muonic boson limits: Supernova redux, *Phys. Rev. D* **105**, 035022 (2022).
- [20] J. B. Dent, B. Dutta, D. Kim, S. Liao, R. Mahapatra, K. Sinha, and A. Thompson, New directions for axion searches via scattering at reactor neutrino experiments, *Phys. Rev. Lett.* **124**, 211804 (2020).
- [21] D. Aristizabal Sierra, V. De Romeri, L. J. Flores, and D. K. Papoulias, Axionlike particles searches in reactor experiments, *JHEP* **03**, 294 (2021).
- [22] A. A. Aguilar-Arevalo et al., (CCM Collaboration), Prospects for detecting axionlike particles at the Coherent CAPTAIN-Mills experiment, *Phys. Rev. D* **107**, 095036 (2023).
- [23] S.-H. Seo et al., Physics Potential of a Few Kiloton Scale Neutrino Detector at a Deep Underground Lab in Korea, [arXiv:2309.13435](https://arxiv.org/abs/2309.13435).
- [24] J. J. Choi et al., (NEON Collaboration), Exploring coherent elastic neutrino-nucleus scattering using reactor electron antineutrinos in the NEON experiment, *Eur. Phys. J. C* **83**, 226 (2023).
- [25] J. J. Choi et al., (NEON Collaboration), Upgrade of NaI(Tl) crystal encapsulation for the NEON experiment, [arXiv:2404.03691](https://arxiv.org/abs/2404.03691).
- [26] G. Adhikari et al., The COSINE-100 liquid scintillator veto system, *Nucl. Instrum. Meth. A* **1006**, 165431 (2021).
- [27] J. J. Choi, B. J. Park, C. Ha, K. W. Kim, S. K. Kim, Y. D. Kim, Y. J. Ko, H. S. Lee, S. H. Lee, and S. L. Olsen, Improving the light collection using a new NaI(Tl) crystal encapsulation, *Nucl. Instrum. Meth. A* **981**, 164556 (2020).
- [28] G. Adhikari et al., (COSINE-100 Collaboration), The COSINE-100 Data Acquisition System, *JINST* **13**, P09006 (2018).
- [29] G. Adhikari et al., (COSINE-100 Collaboration), Background modeling for dark matter search with 1.7 years of COSINE-100 data, *Eur. Phys. J. C* **81**, 837 (2021).
- [30] G. Adhikari et al., (COSINE-100 Collaboration), Lowering the energy threshold in COSINE-100 dark matter searches, *Astropart. Phys.* **130**, 102581 (2021).
- [31] E. Barbosa de Souza et al., (COSINE-100 Collaboration), Study of cosmogenic radionuclides in the COSINE-100 NaI(Tl) detectors, *Astropart. Phys.* **115**, 102390 (2020).
- [32] C. Ha et al., Radon concentration variations at the Yangyang underground laboratory, *Front. in Phys.* **10**, 1030024 (2022).
- [33] M. Roos, Sources of gamma radiation in a reactor core, *J. Nucl. Energy Part B. Reactor Technol.* **1**, 98–104 (1959).
- [34] H. Bechteler, H. Faissner, R. Yogeshwar, and H. Seyfarth, The spectrum of  $\gamma$  radiation emitted in the frj-1 (merlin) reactor core and moderator region, 1984. [Juel-Spez-255](https://arxiv.org/abs/1908.0255).
- [35] H. Primakoff, Photo-production of neutral mesons in nuclear electric fields and the mean life of the neutral meson, *Phys. Rev.* **81**, 899–899 (1951).
- [36] H. M. Chang et al., (TEXONO Collaboration), Search of axions at the Kuo-Sheng nuclear power station with a high-purity germanium detector, *Phys. Rev. D* **75**, 052004 (2007).
- [37] G. Adhikari et al., (COSINE-100 Collaboration), Search for Boosted Dark Matter in COSINE-100, *Phys. Rev. Lett.* **131**, 201802 (2023).
- [38] J.-F. Fortin, H.-K. Guo, S. P. Harris, D. Kim, K. Sinha, and C. Sun, Axions: From magnetars and neutron star mergers to beam dumps and BECs, *Int. J. Mod. Phys. D* **30**, 2130002 (2021).
- [39] B. Batell et al., Dark Sector Studies with Neutrino Beams, in *Snowmass 2021*, 7, 2022. [arXiv:2207.06898](https://arxiv.org/abs/2207.06898).
- [40] L. Di Luzio, M. Giannotti, E. Nardi, and L. Visinelli, The landscape of QCD axion models, *Phys. Rept.* **870**, 1–117 (2020).
- [41] J. Jaeckel and M. Spannowsky, Probing MeV to 90 GeV axion-like particles with LEP and LHC, *Phys. Lett. B* **753**, 482–487 (2016).
- [42] J. Blumlein et al., Limits on the mass of light (pseudo)scalar particles from Bethe-Heitler  $e^+e^-$  and  $\mu^+\mu^-$  pair production in a proton - iron beam dump experiment, *Int. J. Mod. Phys. A* **7**, 3835–3850 (1992).
- [43] A. Payez, C. Evoli, T. Fischer, M. Giannotti, A. Mirizzi, and A. Ringwald, Revisiting the SN1987A gamma-ray limit on ultralight axion-like particles, *JCAP* **02**, 006 (2015).
- [44] J. Jaeckel, P. C. Malta, and J. Redondo, Decay photons from the axionlike particles burst of type II supernovae, *Phys. Rev. D* **98**, 055032 (2018).
- [45] P. Carezza, O. Straniero, B. Döbrich, M. Giannotti, G. Lucente, and A. Mirizzi, Constraints on the coupling with photons of heavy axion-like-particles from Globular Clusters, *Phys. Lett. B* **809**, 135709 (2020).
- [46] J. D. Bjorken, S. Ecklund, W. R. Nelson, A. Abashian, C. Church, B. Lu, L. W. Mo, T. A. Nunamaker, and P. Rassmann, Search for Neutral Metastable Penetrating Particles Produced in the SLAC Beam Dump, *Phys. Rev. D* **38**, 3375 (1988).
- [47] D. J. Bechis, T. W. Dombeck, R. W. Ellsworth, E. V. Sager, P. H. Steinberg, L. J. Teig, J. K. Yoh, and R. L. Weitz, Search for Axion Production in Low-energy Electron Bremsstrahlung, *Phys. Rev. Lett.* **42**, 1511 (1979). [Erratum: *Phys.Rev.Lett.* **43**, 90 (1979)].
- [48] E. M. Riordan et al., A Search for Short Lived Axions in an Electron Beam Dump Experiment, *Phys. Rev. Lett.* **59**, 755 (1987).
- [49] G. Lucente and P. Carezza, Supernova bound on axionlike particles coupled with electrons, *Phys. Rev. D* **104**, 103007 (2021).
- [50] E. Hardy and R. Lasenby, Stellar cooling bounds on new light particles: plasma mixing effects, *JHEP* **02**, 033 (2017).
- [51] S. N. Gninenko, D. V. Kirpichnikov, M. M. Kirsanov, and N. V. Krasnikov, The exact tree-level calculation of the dark

- photon production in high-energy electron scattering at the CERN SPS, *Phys. Lett. B* **782**, 406–411 (2018).
- [52] Y. J. Ko et al., (NEOS Collaboration), Sterile Neutrino Search at the NEOS Experiment, *Phys. Rev. Lett.* **118**, 121802 (2017).
- [53] L. Swiderski, Response of doped alkali iodides measured with gamma-ray absorption and Compton electrons, *Nucl. Instrum. Meth. A* **705**, 42 (2013).
- [54] S. M. Lee et al., (COSINE-100 Collaboration), Nonproportionality of NaI(Tl) scintillation detector for dark matter search experiments, *Eur. Phys. J. C* **84**, 484 (2024).
- [55] J. Amaré, S. Cebrián, C. Cuesta, E. García, C. Ginestra, M. Martínez, M. Oliván, Y. Ortigoza, A. O. de Solórzano, C. Pobes, J. Puimedón, M. Sarsa, J. Villar, and P. Villar, Cosmogenic radionuclide production in nai(tl) crystals, *JCAP* **2015**, 046 (2015).
- [56] P. Villar, J. Amaré, S. Cebrián, I. Coarasa, E. García, M. Martínez, M. A. Oliván, Y. Ortigoza, A. Ortiz de Solórzano, J. Puimedón, M. L. Sarsa, and J. A. Villar, Study of the cosmogenic activation in nai(tl) crystals within the anais experiment, *Int. J. Mod. Phys. A* **33**, 1843006 (2018).
- [57] X. Li, B. Zheng, Y. Wang, and X. Wang, A study of daily and seasonal variations of radon concentrations in underground buildings, *J. Environ. Radioact.* **87**, 101–106 (2006).
- [58] M. Wojcik, W. Wlazole, G. Zuzel, and G. Heusser, Radon diffusion through polymer membranes used in the solar neutrino experiment Borexino, *Nucl. Instrum. Meth. A* **449**, 158–171 (2000).
- [59] A. Arvanitaki, S. Dimopoulos, S. Dubovsky, N. Kaloper, and J. March-Russell, String axiverse, *Phys. Rev. D* **81**, 123530 (2010).
- [60] M. Cicoli, M. D. Goodsell, and A. Ringwald, The type iib string axiverse and its low-energy phenomenology, *JHEP* **2012**, 146 (2012).
- [61] Xcom: Photon cross sections database, <https://www.nist.gov/pml/xcom-photon-cross-sections-database>. Accessed: 2024-04-30.
- [62] F. T. Avignone III, R. L. Brodzinski, S. Dimopoulos, G. D. Starkman, A. K. Drukier, D. N. Spergel, G. Gelmini, and B. W. Lynn, Laboratory Limits on Solar Axions From an Ultralow Background Germanium Spectrometer, *Phys. Rev. D* **35**, 2752 (1987).
- [63] G. Bellini et al., Search for solar axions emitted in the m1-transition of  $7\text{Li}^*$  with borexino ctf, *Eur. Phys. J. C* **54**, 61–72 (2008).
- [64] L. Lyons, Raster scan or 2-D approach?, [arXiv:1404.7395](https://arxiv.org/abs/1404.7395).

## APPENDIX

### NEON detector

The NEON experimental setup [24] was installed in the tendon gallery of reactor unit-6 at the Hanbit nuclear power complex in Yeonggwang, Korea. The location and distance from the reactor core are similar to those in the NEOS experiment [52], which was installed in reactor unit-5 within the same complex. The detector is located approximately  $23.7 \pm 0.3$  m from the center of the reactor core, as shown in Fig. A1.

The NEON detector is contained within a 4-layer nested arrangement of shielding components of a polyethylene castle, a borated polyethylene board, a lead castle, and linear alkylbenzene-based liquid scintillator as shown in Fig. A1. The six NaI(Tl) crystal assemblies are placed inside of the liquid scintillator.

Physics data collection commenced on April 11, 2022, following an upgrade of crystal encapsulation [25]. Generally, data were collected stably, albeit with a few downtime periods caused by unexpected power outages. These outages led to failure in the high voltage supply crate and malfunctions in a DAQ module. Due to the lack of an online connection, to ensure the security of reactor operations, downtime periods in the summer 2022 were extended.

At the beginning of the physics operations, we collected data with the reactor operating at full power (reactor-on data) for 120 days. Due to the unexpected power outage, the NEON DAQ system was offline for 38 days during this period. The reactor was inactive from September 26, 2022, to February 22, 2023, for regular maintenance and fuel replacement. During this period, we collected reactor-off data for 144 days. After regular maintenance, the reactor resumed operation on February 22, 2023. There were approximately 3-day periods of ramping down (September 23–26) and ramping up (February 22–25) associated with the change in reactor operations that were not used to avoid the complexity of photon and ALP fluxes. After the reactor restarted, it has been running stably at full power. We used data collected up until June 22, 2023, adding 117 days of reactor-on data.

### Data process

An event that satisfies the trigger condition of coincident photoelectrons in both of the crystal's readout PMTs within 200 ns is acquired using 500 MHz flash analog-to-digital converters (FADCs) and recorded as an  $8 \mu\text{s}$  long waveform starting  $2.4 \mu\text{s}$  before the trigger occurs. To reduce the high trigger rate caused by muon phosphorus events, an event veto logic is implemented that applies a 300 ms dead time for energy deposits exceeding approximately 3 MeV in each crystal. This veto logic results in a dead time of approximately 10 % for 8-inch crystals and 5 % for 4-inch crystals [24]. We have monitored the rate of the muon candidate events and evaluated the exact dead time for each an hour dataset.

The energy scales and resolutions are determined by calibration using internal  $\beta$ - and  $\gamma$ -ray peaks from radioactive contaminants in the crystals, as well as external sources. For external  $\gamma$ -ray calibrations,  $^{241}\text{Am}$  and  $^{22}\text{Na}$  sources in a stainless-steel case suitable for the calibration tube were prepared using standard isotope solutions with approximately 100 Bq activities. These sources were installed in the calibration holes to provide  $\gamma$ -ray energies of 59.54 keV, 511 keV, and 1275 keV for both NaI(Tl) crystals and liquid scintillator calibrations [24]. Internal contaminant peaks at 49 keV ( $^{210}\text{Pb}$ ), 238 keV ( $^{212}\text{Pb}$ ), 295 and 352 keV ( $^{214}\text{Pb}$ ), 1173 keV ( $^{60}\text{Co}$ ), 1462 keV ( $^{40}\text{K}$ ), 1764 keV and 2204 keV ( $^{214}\text{Bi}$ ), and 2614 keV ( $^{208}\text{Tl}$ ) were used to calibrate the NaI(Tl) crystals, following a method similar to that used in the COSINE-100 experiment [29]. Nonlinear responses of the NaI(Tl) crystals, as studied in Refs. [53, 54] were also accounted for.

In offline analysis, events with energy deposits greater than 5 MeV in the liquid scintillator detector are rejected as muon candidate events. To further reject muon phosphorus events and electronic interference, we require that waveforms from the crystal exhibit more than two single photoelectrons, the integral waveform area below the baseline does not exceed a limit, and leading edges of the trigger pulses start no earlier than  $2.0 \mu\text{s}$  after the recording begins. Alpha-induced events from U or Th contamination are rejected by requiring a charge-weighted average time to be greater than  $2.4 \mu\text{s}$ .

This analysis utilizes events with energies ranging from 3 keV to 3000 keV to avoid unexpected noise contamination, effectively removed by a boosted decision tree (BDT)-based event selection [30]. Although this analysis was not affected by low-energy noise events, the same data quality cut developed for low-energy analyses, such as CE $\nu$ NS searches, was applied. The data quality is monitored for event rates of 1–3 keV energies after applying the BDT-based event selection criteria. The event rate of each one-hour dataset for each detector module is compared with the general rate distribution to classify data as good when the one-hour rate falls within a  $3\sigma$  range of the mean event rate, or as bad for other datasets.

Due to relatively large fluctuations of low-energy event rates from detector-3, we decided to exclude this detector from the ALP search analysis. Table A1 shows the data exposure for each crystal accepted by all criteria, and Fig. A2 presents these exposures in the time domain for each detector module. In total, we used 1596 kg-days reactor-on data and 1467 kg-days reactor-off data for this analysis.

### Time dependent background component

The dominant background contributions remained consistent over the two-years data collection period, characterized as continuum background. Apart from the continuum background, several time-dependent backgrounds contribute differently to the reactor-on and reactor-off data. The cosmogenic contributions in the NaI(Tl) crystal detectors were extensively studied by the ANAIS [55, 56] and COSINE [31] experiments, identifying isotopes such as  $^{125}\text{I}$ ,  $^{121}\text{Te}$ ,  $^{123m}\text{Te}$ ,  $^{125m}\text{Te}$ ,  $^{127m}\text{Te}$ ,  $^{113}\text{Sn}$ ,  $^{22}\text{Na}$  and  $^3\text{H}$ , which



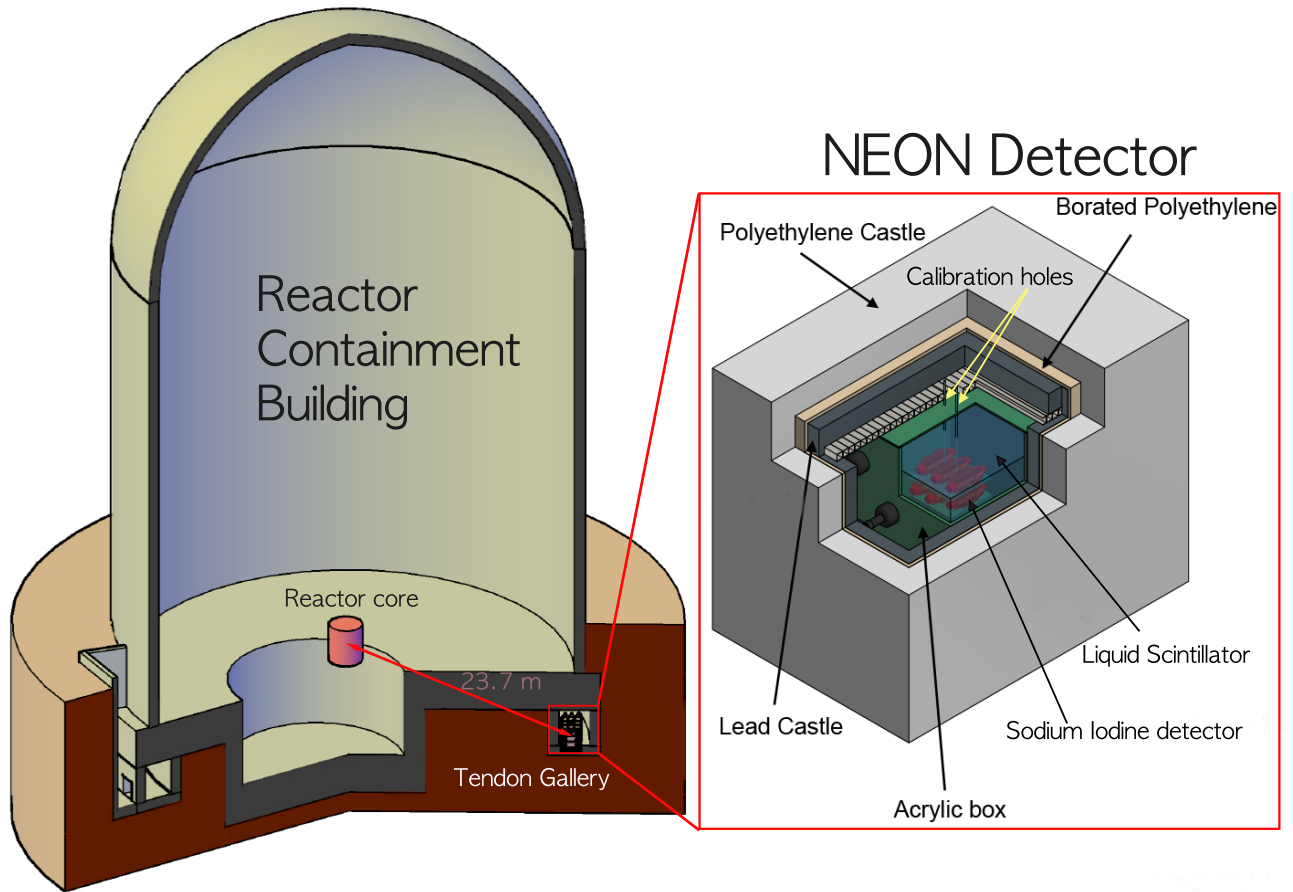


Fig. A1. **Schematic view of the NEON detector.** The NEON detector is positioned 23.7 m from the reactor core of Hanbit nuclear power complex unit-6, which has a 2.8GW thermal power capacity. It comprises six NaI(Tl) detector modules surrounded by 800 L of liquid scintillator, a 10 cm-thick layer of lead, a 3 cm-thick borated polyethylene, and a 20 cm-thick high-density polyethylene.

TABLE A1. **Summary of good quality data.** This table summarizes the data used for the ALP searches in each detector module, categorized separately for reactor-on and -off periods. All data from detector-3 were excluded from this analysis due to contamination from low-energy noise.

Detector	Mass	reactor-on data	reactor-off data
detector-1	1.67 kg	165.4 kg-days	201.2 kg-days
detector-2	3.34 kg	413.4 kg-days	352.3 kg-days
detector-3	1.67 kg	–	–
detector-4	3.34 kg	527.9 kg-days	367.6 kg-days
detector-5	3.35 kg	160.2 kg-days	279.8 kg-days
detector-6	3.35 kg	329.4 kg-days	266.0 kg-days
Total	16.72 kg	1596.3 kg-days	1466.9 kg-days

mainly contributed energies below 100 keV. Due to relatively long half-life of  $^{22}\text{Na}$  (2.6 years) and  $^3\text{H}$  (12.3 years), their contributions persist across all detectors. However, short-lived components with a half-life of less than a year decayed following the initial installation in December 2020. The initial

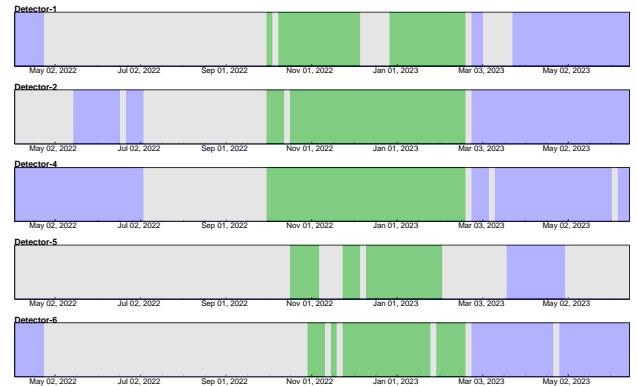
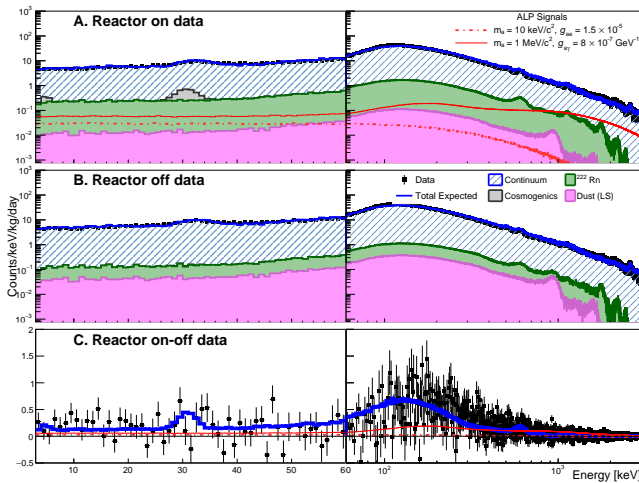


Fig. A2. **Good quality data used for the ALP search in time domain.** We present the good quality data as a function of time for each detector module. reactor-on data is represented in blue, -off data in green, and periods of DAQ downtime or bad quality data are marked in gray.

data from the two new detector modules, detector-5 and 6, were significantly influenced by short-lived cosmogenic iso-



**Fig. A3. Multiple-hit energy spectra of the detector-6 module.** This figure shows the normalized energy spectra of the multiple-hit events (black points) in the detector-6 module. The spectra are compared with the expected background contributions (blue solid lines) for both the reactor-on state (A) and the reactor-off state (B). The expected background includes contributions from time-independent continuum components and time-dependent components of cosmogenic activation,  $^{222}\text{Rn}$  in the calibration hole, and  $^{238}\text{U}$   $^{232}\text{Th}$  from the dust contamination in the liquid scintillator. For the reactor-on data (A), two benchmark ALP signals of  $m_a = 10 \text{ keV}/c^2$ ,  $g_{ae} = 1.5 \times 10^{-5}$  (red dashed line) and  $m_a = 1 \text{ MeV}/c^2$ ,  $g_{a\gamma} = 8 \times 10^{-7} \text{ GeV}^{-1}$  (red solid line) are included. (C) shows the reactor-on-minus-off data spectrum with the expected background (blue solid line) and the same two benchmark ALP signals.

topes. Detector-1 experienced relatively large contributions from cosmogenic activation due to approximately one year of additional exposure to muons during R&D of the detector encapsulation. By considering the data exposure times seen in Fig. A2 and the half-life of each isotope, we could model the cosmogenic contributions for each detector module.

Another source of time-dependent background is the seasonal variation of  $^{222}\text{Rn}$ , which has been reported to be higher during the summer and lower during the winter [32, 57]. The NEOS experiment measured  $^{222}\text{Rn}$  using a Radon eye device in the tendon gallery, demonstrating clear variations with high levels in summer and lower levels in winter (see Fig. A5). Initially the NEON experiment did not employ a  $^{222}\text{Rn}$  measurement device. However, in December 2023, a Radon eye was installed to monitor the  $^{222}\text{Rn}$  levels in the tendon gallery.

The NEON detector features two calibration holes connected from the top of the shield to the vicinity of the crystal modules, as indicated in Fig. A1. These calibration holes were opened and exposed to the same level of  $^{222}\text{Rn}$  as the experimental tunnel. As observed from seasonal variations of  $^{222}\text{Rn}$  in the tendon gallery in the NEOS experiment, this could influence the seasonal changes in observed background levels in the NEON experiment. We simulated spectra from  $^{222}\text{Rn}$  in the calibration holes, with the largest contributions found in the 100–500 keV range of multiple-hit events (see Fig. A4 (A)). The summer data exhibited a clearly enhanced

rate compared to winter data, primarily due to seasonal variations in  $^{222}\text{Rn}$ . Since our reactor-off data were predominantly collected in winter season, as shown in Fig. A2, the seasonal variation of  $^{222}\text{Rn}$  contributed to larger background for the reactor-on data.

Another source of time-dependent background is dust within the liquid scintillator. The environmental conditions of the tendon gallery were not sufficiently clean. During the initial installation, we conducted all installation quickly to avoid dust contamination and installed a vinyl house to prevent additional dust from entering the detector. However, the upgrade of detector encapsulation was pursued due to instability issues [25]. This process took about a year of R&D using the detector-1 module to upgrade the encapsulation and reinstall the upgraded module. Multiple modifications to the encapsulation design and test measurements inside the shield required multiple opening of the system. Due to limited space of the tendon gallery, the temporal vinyl house had to be removed to access the system. These steps continuously contaminated the dust within the liquid scintillator, which contained long-lived isotopes such as  $^{238}\text{U}$ ,  $^{232}\text{Th}$ , and  $^{40}\text{K}$ . Initially, the dust might have been suspended in the middle of the liquid scintillator and settled at the bottom of the container over time, resulting in reduced contributions. We simulated spectra from the dust in the liquid scintillator.

To identify the time-dependent background in our data, we divided the data into seven different time periods, each two-month long, and fitted the data with expected background spectra. Here, we extended the data set until August 2023 to capture the maximum contribution of  $^{222}\text{Rn}$ . Figure A4 provides two examples of the multiple-hit spectra of the detector-6 module from data taken between June 15 and August 15, 2022 (B), and between January 1 and February 28, 2023 (C), which exhibited the most distinct rate (shown in (A)). For each of seven distinct data sets, we simultaneously performed background model fitting for the single-hit and the multiple-hit data. The fitted  $^{222}\text{Rn}$  and dust contributions are shown in Fig. A5 as the averaged rate between 100 keV and 500 keV for the multiple-hit events. We also compared the evaluated  $^{222}\text{Rn}$  activities with the the measured activities in the NEOS experimental site, finding an excellent match despite the NEOS Radon eye measurements being conducted in different years and tunnels. We observed a decreased rate of liquid scintillator dust contributions, which could be attributed to the settling of dust at the bottom.

### Systematic uncertainties

Various sources of systematic uncertainties are taken into account. Errors associated with the energy resolution, the energy scale, and background modeling technique were translated into shape or rate changes of the reactor-on-minus-off spectra. We considered a maximum variation assuming opposite-side variations between the reactor-on and reactor-off data, as exemplified by the energy resolution in Fig. A6. These quantities are allowed to vary within their uncertainties as nuisance parameters in the ALP signal fit.

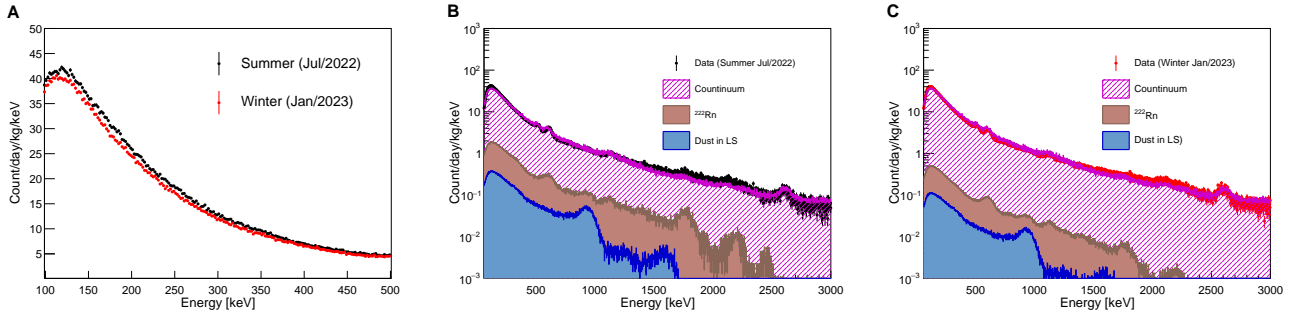


Fig. A4. **Time-dependent background models for multiple-hit events in detector-6.** (A) displays a noticeable difference in event rates between the summer (15 June 2022 – 15 August 2022) and winter (1 January 2023 – 28 February 2023) seasons, attributed to the seasonal variation of  $^{222}\text{Rn}$ . Data from summer (B) and winter (C) are modeled with the time-independent continuum and time-dependent contributions from  $^{222}\text{Rn}$  and liquid scintillator dust, allowing us to quantify the amounts of these time-dependent components.

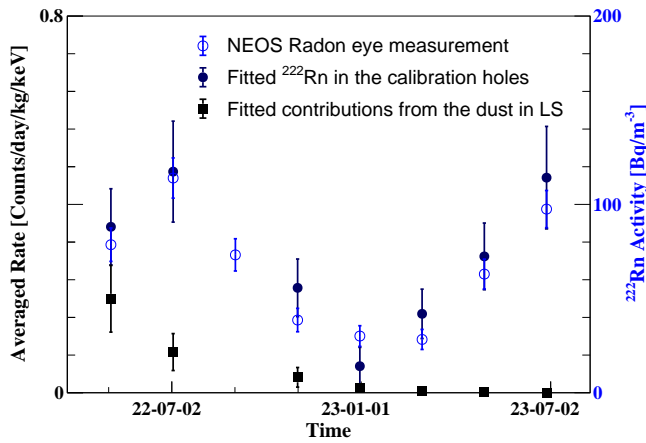


Fig. A5. **Time-dependent background contributions of  $^{222}\text{Rn}$  and liquid scintillator dust contamination.** Presented are the fitted rates for the multiple hit events in detector-6, averaged at energies between 100 keV and 500 keV. These include contributions from  $^{222}\text{Rn}$  in the calibration holes (dark blue filled circles) and from liquid scintillator dust (black filled squares). Also shown are the measured  $^{222}\text{Rn}$  activities (right axis), from the NEOS tunnel using a Radon eye device (blue open circles), corresponding to the same seasons, although these measurements were conducted in different years and in the tendon gallery of reactor unit-5 (while NEON is located at reactor unit-6). Despite the differences in location and year, there is excellent agreement in the seasonal variations of  $^{222}\text{Rn}$  between the NEOS Radon eye measurements and the NEON data.

The dominant systematic uncertainties are related with the time-dependent background modeling of  $^{222}\text{Rn}$  and liquid scintillator dust contributions. Approximately 30% uncertainties were extracted from the amount of the time-dependent background, as shown in Fig. A4. In addition to the rate variation, we considered the possibility of shape changes due to different locations of the  $^{222}\text{Rn}$  contamination. Although we considered the background contribution of  $^{222}\text{Rn}$  only from the calibration holes,  $^{222}\text{Rn}$  could be permeable and diffused in the liquid scintillator [58]. Due to different  $^{222}\text{Rn}$  contaminant positions from the NaI(Tl) detector modules, this could

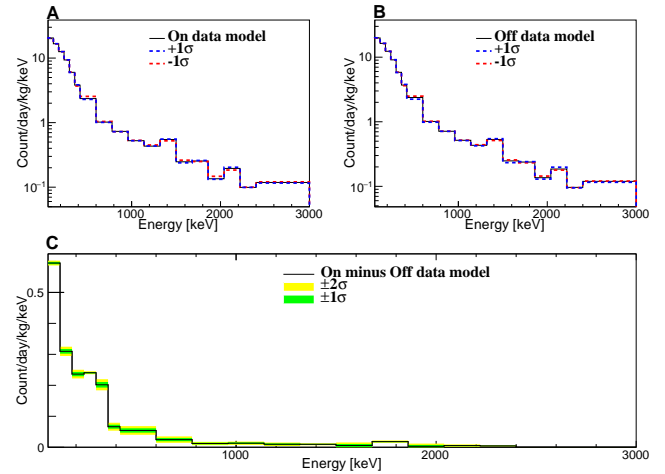


Fig. A6. **Systematic uncertainty due to energy resolution.** Uncertainty in energy resolution, derived from internal or external  $\gamma$  lines, is propagated into the best model (solid line) of the single-hit events for detector-6 across the energy range of 60–3000 keV, as indicated by dashed lines. Variations in the reactor-on data (A) and -off data (B) are carried over into reactor-on-minus-off data spectrum (C), showing maximum deviations depicted by green ( $1\sigma$ ) and yellow ( $2\sigma$ ) uncertainty bands.

result in different background spectra, as observed in Fig. A7. These types of shape changes were accounted as the systematic uncertainties.

We modeled the contributions of liquid scintillator dust contributions with background spectra generated homogeneously in the liquid scintillator and accounted for rate changes by modeling two-months period data. In addition to a 30% level rate variation, we considered shape changes resulting from different locations. We divided the contaminant locations in the liquid scintillator into six different regions from top to bottom and accounted for the maximum shape variations as the systematic uncertainty.

Figures 2, A8 and, A9 show the reactor-on-minus-off data spectra compared with the expected background, including the associated systematic uncertainty bands. As can be seen

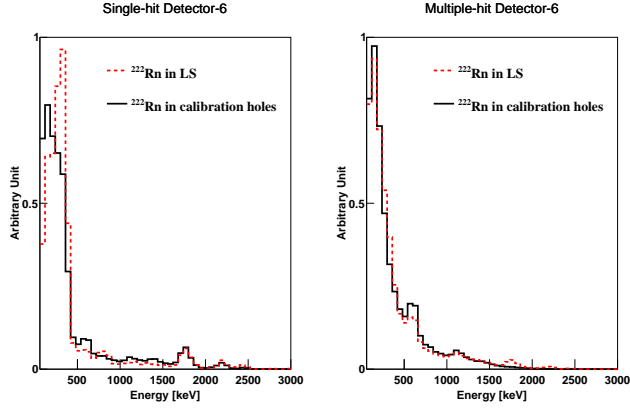


Fig. A7. **Systematic uncertainty of  $^{222}\text{Rn}$  shape.** Normalized background spectra for the detector-6 module originating from  $^{222}\text{Rn}$  are presented separately for the single-hit events and the multiple-hit events. The spectra compare two different locations of the calibration holes and the liquid scintillator. The observed shape differences are considered as the systematic uncertainty of  $^{222}\text{Rn}$ , in addition to 30% of rate variation.

from these figures, our data spectra were well described by the expected time-dependent backgrounds within their systematic uncertainties.

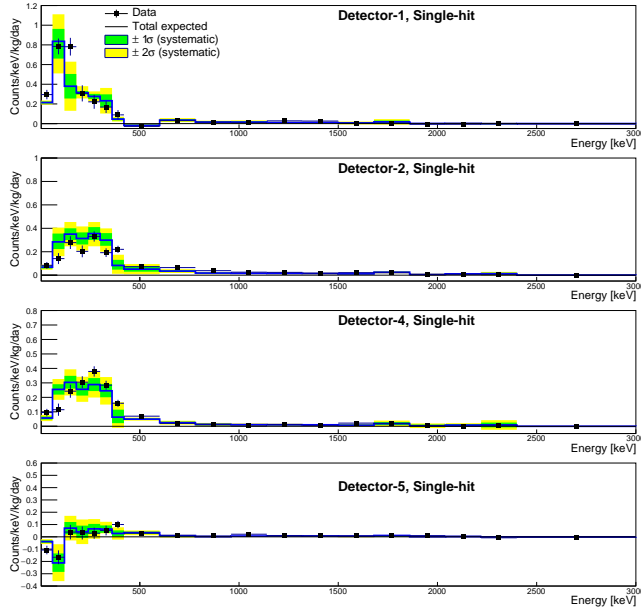


Fig. A8. **Single-hit data used for ALP search.** This figure present the single-hit energy spectra of the reactor-on-minus-off data used for ALP signal searches (Fig. 2 (A) for detector-6). The data points (black circles) are well agreed with the expected background spectra (blue solid lines) within assigned uncertainties (green and yellow bands).

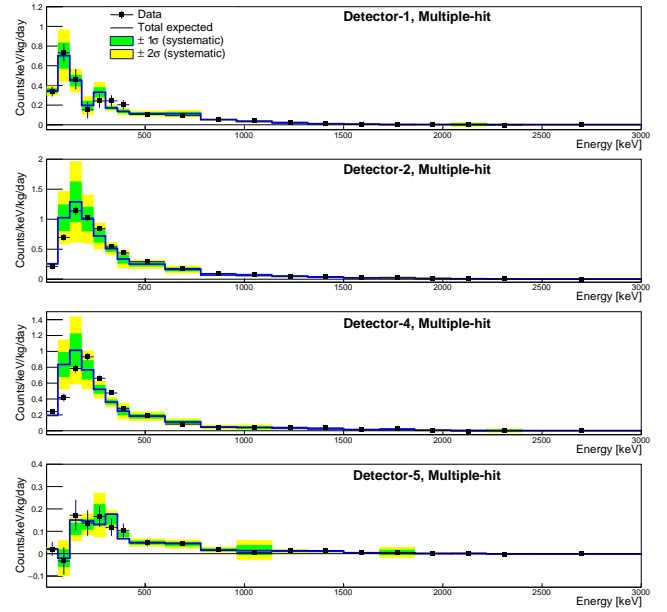


Fig. A9. **Multiple-hit data used for ALP search.** This figure present the multiple-hit energy spectra of the reactor-on-minus-off data used for ALP signal searches (Fig. 2 (B) for detector-6). The data points (black circles) are well agreed with the expected background spectra (blue solid lines) within assigned uncertainties (green and yellow bands).

## Signal generation

The nuclear reactor cores produce a huge number of photons, which can scatter off the fuel material within the reactor tank to produce ALPs [33]. We use a reactor photon flux approximation derived from the FRJ-1 research reactor [34] as follows,

$$\frac{d\Phi_\gamma}{dE_\gamma} = \frac{5.8 \times 10^{17}}{[\text{MeV}] \cdot [\text{sec}]} \left( \frac{P}{[\text{MW}]} \right) e^{-1.1E_\gamma/[\text{MeV}]}, \quad (1)$$

where  $P$  is the thermal power and  $E_\gamma$  denotes the energy of photons. The uncertainty of the photon flux can systematically alter the expected ALP signal rate. Although a maximum of 10% uncertainty in photon flux has been considered, the impacts on the coupling constant would be negligibly affected [21].

Here, we consider the generic model where the ALP can couple to either a photon or an electron [59, 60]. With non-zero ALP-photon coupling constant  $g_{a\gamma}$  and ALP-electron coupling constant  $g_{ae}$ , ALPs can be produced via the Primakoff process  $\gamma + A \rightarrow a + A$  [35] and the Compton-like process  $\gamma + e^- \rightarrow a + e^-$  [21], respectively. Once produced within the reactor core, ALPs propagate through the shielding material until they either decay in flight or reach to the detector material. The ALP flux at the detector can be described by the following convolution, taking into account decays in

flight [21],

$$\frac{d\Phi_a^P}{dE_a} = P_{\text{surv}} \int_{E_{\gamma, \min}}^{E_{\gamma, \max}} \frac{1}{\sigma_{SM} + \sigma_{P(C)}} \frac{d\sigma_{P(C)}^P}{dE_a} (E_{\gamma}, E_a) \times \frac{d\Phi_{\gamma}}{dE_{\gamma}} dE_{\gamma}, \quad (2)$$

where  $\sigma_{SM}$  represents the total photon scattering cross-section against core material, referenced from the Photon Cross Sections Database [61],  $E_a$  represents the energy of the ALP, and  $\sigma_{P(C)}^P$  denotes the production cross-section for the Primakoff process (Compton-like process) [21].

The ALP survival probability  $P_{\text{surv}}$ , assuming that the ALP flux reaches the detector, is given by [20],

$$P_{\text{surv}} = e^{-LE_a/p_a\tau}, \quad (3)$$

where  $L$  denotes the distance between reactor core and the detector,  $p_a$  represents the ALP momentum, and  $\tau$  is the ALP lifetime in the fixed target frame, determined in term of the ALP total decay width,

$$\Gamma(a \rightarrow \gamma\gamma) = \frac{g_{a\gamma}^2 m_a^3}{64\pi} \quad (4)$$

$$\Gamma(a \rightarrow e^+e^-) = \frac{g_{ae}^2 m_a}{8\pi} \sqrt{1 - 4\frac{m_e^2}{m_a^2}}, \quad (5)$$

where  $m_a$  is the ALP mass and  $m_e$  is electron mass.

In case of non-zero  $g_{a\gamma}$ , the ALP could be detected through the inverse Primakoff process  $a + A \rightarrow \gamma + A$  or two photon pair decay  $a \rightarrow \gamma\gamma$  in the detector material. The expected signal events can be expressed as,

$$\frac{dN_{a\gamma}}{dE_a} = m_{\text{det}} \frac{N_{\text{target}}}{4\pi L^2} \sigma_D^P \frac{d\Phi_a^P}{dE_a} + \frac{A}{4\pi L^2} \frac{d\Phi_a^P}{dE_a} P_{\text{decay}}, \quad (6)$$

where  $m_{\text{det}}$  represents the total mass of detector,  $N_{\text{target}}$  denotes the ratio of the Avogadro number to the number of target nuclei, and  $\sigma_D^P$  is the total inverse-Primakoff scattering cross section, which has twice the value of  $\sigma_D^P$  due to the initial spin state including a spin-0 ALP rather than a spin-1 photon.  $A$  stands for the detector transverse area, and  $P_{\text{decay}}$  accounts for the probability that the decay occurs within the detector as follows

$$P_{\text{decay}} = 1 - e^{-L_{\text{det}} E_a / |p_a| \tau}, \quad (7)$$

where  $L_{\text{det}}$  denotes the detector length.

In case of non-zero  $g_{ae}$ , we consider inverse-Compton-like process  $a + e^- \rightarrow \gamma + e^-$ , Axio-electric absorption  $a + e^- + N \rightarrow e^- + N$  [62], and electron-positron pair decay  $a \rightarrow e^+e^-$ . The expected event rate for each process can be expressed as,

$$\frac{dN_C^C}{dE_a} = m_{\text{det}} \frac{N_{\text{target}}}{4\pi L^2} \sigma_D^C \frac{d\Phi_a^C}{dE_a} + m_{\text{det}} \frac{N_{\text{target}}}{4\pi L^2} \sigma_D^A \frac{d\Phi_a^C}{dE_a} + \frac{A}{4\pi L^2} \frac{d\Phi_a^P}{dE_a} P_{\text{decay}}, \quad (8)$$

where  $\sigma_D^C$  and  $\sigma_D^A$  are inverse Compton process cross section and Axio-electron cross section, respectively, described in detail in Refs. [21, 63]. Figure A10 shows the expected event

rate in the NaI(Tl) crystals for each detection process through the above calculations. In these energy spectra, sum energy of produced standard model particles such as electron, positron, and photon in the NaI(Tl) crystals are taken into account.

ALP signals for each detection process in the mass range from 1 eV/c<sup>2</sup> to 10 MeV/c<sup>2</sup> are simulated. Calculated ALP fluxes in the reactor are generated within the volume of the reactor core and propagate to the NEON detector isotropically, utilizing the geometry shown in Fig. A1 to account for the direction and momentum of the ALP events. When the ALPs reach to the detector volume, which includes the liquid scintillator and the NaI(Tl) crystals, we simulate each ALP interaction, considering scattering or decay processes for each coupling. Produced electrons/positrons and photons are processed for detector responses using Geant4-based simulation. Figure A11 illustrates the expected ALP signals for a few benchmark signals in the single-hit (A) and the multiple-hit (B) events.

Typically, the  $a \rightarrow e^+e^-$  and Axio-electric processes result in electrons and positron in the detector with energies less than a few MeV. In this situation, mostly single detector absorbs all energies, resulting in single-hit events. Other processes, including MeV-energy photons, can deposit energies in the multiple detectors through the Compton process, resulting in the multiple-hit events, as shown in Fig. A11.

### ALP signal fit

To extract the ALP signal from the NEON data, a  $\chi^2$  fit is performed with a  $\chi^2$  function defined as,

$$\chi^2 = \sum_i^{10} \sum_j \frac{[M_{ij}(\tau_i^{\text{on}}, \tau_i^{\text{off}}) - B_{ij}(\boldsymbol{\alpha}, \boldsymbol{\beta}) - S_{ij}(\boldsymbol{\alpha}, m_a)]^2}{\sigma_{ij}(\tau_i^{\text{on}}, \tau_i^{\text{off}})}, \quad (9)$$

where index  $i$  represents crystal and channel (single-hit and multiple-hit) numbers, and  $j$  denote the energy bin, respectively.  $M_{ij}(\tau_i^{\text{on}}, \tau_i^{\text{off}})$  represents the normalized rate of reactor-on data subtracted by reactor-off data for crystal (and channel)  $i$  in the  $j^{\text{th}}$  energy bin, scaled by reactor-on period  $\tau_i^{\text{on}}$  and reactor-off period  $\tau_i^{\text{off}}$ . The the number of background  $B_{ij}(\boldsymbol{\alpha}, \boldsymbol{\beta})$  and signal events  $S_{ij}(\boldsymbol{\alpha}, m_a)$  come from the time-dependence background modeling and ALP signal discussed above. Associated uncertainty  $\sigma_{ij}(\tau_i^{\text{on}}, \tau_i^{\text{off}})$  is propagated from data amount of the reactor-on and -off periods. The systematic uncertainty affecting the background model is included as a nuisance parameter  $\boldsymbol{\alpha}$  and  $\boldsymbol{\beta}$ ,

$$B_{ij}(\boldsymbol{\alpha}, \boldsymbol{\beta}) = \prod_k (1 + \alpha_{ik} \cdot \delta b_{ijk}) \sum_l (1 + \beta_{il}) B_{ijl}^{MC}, \quad (10)$$

where the index  $k$  represents systematic uncertainty component, and  $l$  denotes the background component.  $B_{ijl}^{MC}$  is the number of background event obtained by modeling for  $l^{\text{th}}$  background component. The nuisance parameter  $\alpha_{ik}$  controls the effect of the energy-dependent uncertainty ( $\delta b_{ijk}$ ). Meanwhile, another nuisance parameter  $\beta_{il}$  adjusts the activity for

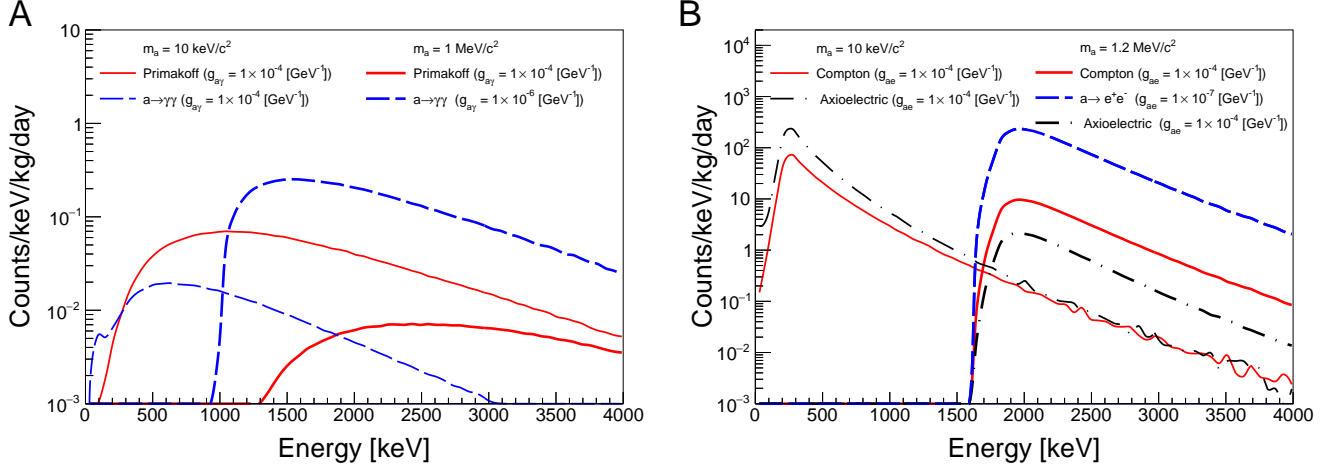


Fig. A10. **Expected ALP events rates for each detection process.** The scatter and decay rates from axion photon coupling (A) and axion electron coupling (B) in the NaI(Tl) crystal are shown for individually chosen values of  $g_{a\gamma}$  and  $g_{ae}$  for the ALP masses of  $10 \text{ keV}/c^2$ ,  $1 \text{ MeV}/c^2$ , and  $1.2 \text{ MeV}/c^2$ .

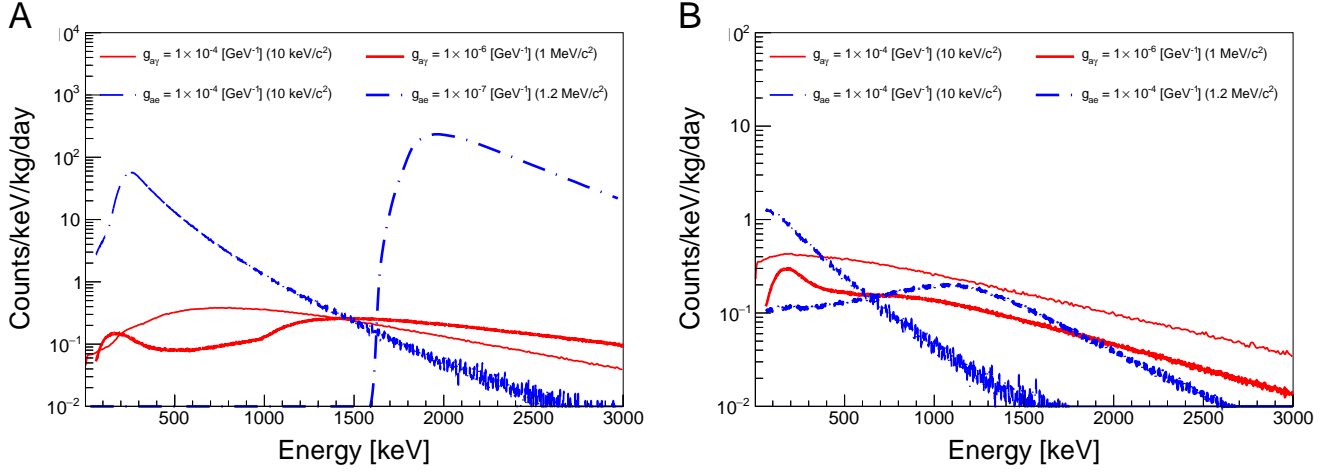


Fig. A11. **Expected ALP signals in the NEON detector.** The expected event rates from the ALP interactions in the NEON detector considering detector responses are presented for the single-hit events (A) and the multiple-hit events (B). Individually chosen values of  $g_{a\gamma}$  and  $g_{ae}$  for the ALP masses of  $10 \text{ keV}/c^2$ ,  $1 \text{ MeV}/c^2$ , and  $1.2 \text{ MeV}/c^2$  are shown.

$l^{\text{th}}$  background component. Similar impact on the ALP signal is considered by means of the expression

$$S_{ij}(\alpha, m_a) = \prod_k (1 + \alpha_{ik} \cdot \delta b_{ijk}) S_{ij}(m_a), \quad (11)$$

where the  $S_{ij}(m_a)$  is the expected rate of ALP- $\gamma$  or ALP-electron interaction in the  $j^{\text{th}}$  energy bin for  $i^{\text{th}}$  crystal obtained after the detector simulation discussed above. Each nuisance parameter is constrained within the evaluated uncertainty with a Gaussian prior.

For each ALP interaction signal, we estimate the probabil-

ity density function (PDF) using a raster scan [64] as follows,

$$\text{PDF} = N e^{-(\chi^2 - \chi_{min}^2)/2}, \quad (12)$$

where  $N$  is the normalization constant ensuring the integration of the PDF equals unity, and  $\chi_{min}^2$  is the minimum  $\chi^2$ . If the most probable value is consistent with null signal, we obtain a 95% confidence level exclusion limit from the integration of the PDF matched to 0.95, as an example shown in Fig. A12 for the ALP signals of  $m_a = 1 \text{ MeV}/c^2$  and the axion-photon coupling.

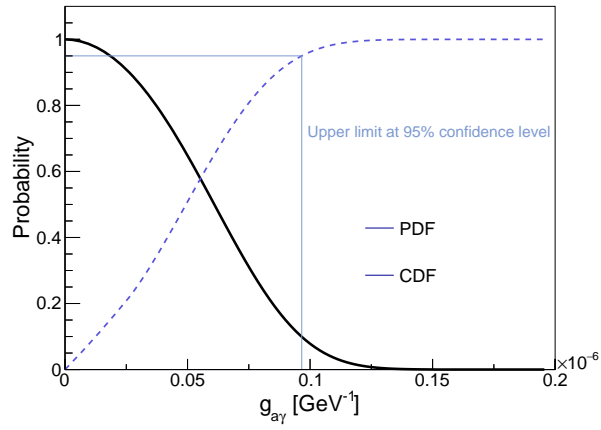


Fig. A12. **An example of the probability density function (PDF) and cumulative density function (CDF).** The PDF and CDF for the ALP signal fit of the axion-photon coupling with  $m_a = 1 \text{ MeV}/c^2$  are presented. The most probable value points to a null signal, and the 95% confidence level upper limit was set by CDF value matched with 0.95.